

Boundary-Layer Development and Low-level Baroclinicity during High-Latitude Cold-Air Outbreaks: A Simple Model

Dmitry G. Chechin¹  · Christof Lüpkes²

Received: 20 August 2015 / Accepted: 13 July 2016 / Published online: 4 August 2016
© Springer Science+Business Media Dordrecht 2016

Abstract A new quasi-analytical mixed-layer model is formulated describing the evolution of the convective atmospheric boundary layer (ABL) during cold-air outbreaks (CAO) over polar oceans downstream of the marginal sea-ice zones. The new model is superior to previous ones since it predicts not only temperature and mixed-layer height but also the height-averaged horizontal wind components. Results of the mixed-layer model are compared with dropsonde and aircraft observations carried out during several CAOs over the Fram Strait and also with results of a 3D non-hydrostatic (NH3D) model. It is shown that the mixed-layer model reproduces well the observed ABL height, temperature, low-level baroclinicity and its influence on the ABL wind speed. The mixed-layer model underestimates the observed ABL temperature only by about 10 %, most likely due to the neglect of condensation and subsidence. The comparison of the mixed-layer and NH3D model results shows good agreement with respect to wind speed including the formation of wind-speed maxima close to the ice edge. It is concluded that baroclinicity within the ABL governs the structure of the wind field while the baroclinicity above the ABL is important in reproducing the wind speed. It is shown that the baroclinicity in the ABL is strongest close to the ice edge and slowly decays further downwind. Analytical solutions demonstrate that the e-folding distance of this decay is the same as for the decay of the difference between the surface temperature of open water and of the mixed-layer temperature. This distance characterizing cold-air mass transformation ranges from 450 to 850 km for high-latitude CAOs.

Keywords Baroclinicity · Cold-air outbreaks · Low-level jet · Mixed-layer model

✉ Dmitry G. Chechin
chechin@ifaran.ru

Christof Lüpkes
Christof.Luepkes@awi.de

¹ A.M. Obukhov Institute of Atmospheric Physics of the Russian Academy of Sciences, Pyzevsky per., 3, Moscow, Russia 119017

² Alfred Wegener Institute Helmholtz Zentrum for Polar and Marine Research, Bussestrasse, 24, 27570 Bremerhaven, Germany

List of Symbols

C_D, C_H	Bulk transfer coefficients of momentum (D) and heat (H)
E_m	Geostrophic Ekman number
f	Coriolis parameter
g	Acceleration due to gravity
H	Atmospheric boundary-layer (ABL) height scale
K	Proportionality constant
K_M, K_H	Eddy diffusivities for momentum (M) and heat (H)
L_{tr}	Characteristic length scale of the air-mass transformation
U_g and V_g	Horizontal components of large-scale geostrophic wind vector
U_{g+}, U_{gi}, U_{gt}	Baroclinic parts of the u -components of the geostrophic wind vector averaged over the ABL height
u_*	Friction velocity
$\mathbf{V}_{gm}, u_{gm}, v_{gm}$	Geostrophic wind vector averaged over the ABL height and its west-east and north-south components, respectively
\mathbf{V}_m, u_m, v_m	Horizontal wind vector averaged over the ABL height and its west-east and north-south components, respectively
u_+ and v_+	Wind vector components right above the inversion
w_e	Entrainment velocity
\bar{y}	Normalized distance from the ice edge along the north-south direction (orthogonal to the ice edge)
\hat{y}	Linear function of \bar{y} ($\hat{y} = C_1\bar{y} - C_2$, where C_1 and C_2 are constants as in Eq. 14)
z_{0m}, z_{0h}	Roughness length for momentum (m) and heat (h)
z_i	ABL height defined as the height of the capping inversion
z_{i+}, z_{i-}	Height just above ($i+$) and below ($i-$) the capping inversion
z_{i0}	ABL height over the sea ice
$(w'\theta')_s$	Vertical kinematic heat flux in the surface layer
α	Angle between the direction of the large-scale geostrophic wind and y -axis
β	Entrainment coefficient
γ_h	Non-local term in the heat-flux parametrization
γ_θ	Potential temperature lapse rate above the ABL
$\Delta\theta$	Discontinuous jump of potential temperature at the ABL top
Δu and Δv	Discontinuous jump of the horizontal components of wind vector u and v , respectively
θ_+	Potential temperature right above the inversion
θ_{ice}	Potential temperature at $z = z_{0h}$ over the sea-ice and also mixed-layer inflow potential temperature
θ'_{ice}	Modified θ_{ice} given by $\theta'_{ice} = \theta_{ice} - \gamma_\theta z_{i0}(1 + \beta)/(1 + 2\beta)$ and used only for normalization of θ_m
θ_w	Potential temperature at $z = z_{0h}$ over the open water
θ_m	Potential temperature averaged over the ABL height
ϕ	Angle between the direction of the ABL-averaged wind vector and y -axis

1 Introduction

Marine cold-air outbreaks (CAOs) are typical wintertime meteorological phenomena over ocean areas at high latitudes. They play an important role in the polar climate system since they are associated with extremely strong energy exchange between the ocean and atmosphere. This exchange takes place over large areas downstream of the pack ice and marginal sea-ice zone and influences air and water masses as well as sea-ice thermodynamics in the marginal sea-ice zone.

CAOs are driven by synoptic-scale processes and have a horizontal scale comparable to that of synoptic systems. However, CAOs also produce favourable conditions for motions of various scales such as convective rolls and cells (e.g., [Renfrew and Moore 1999](#); [Brümmer and Pohlmann 2000](#)), baroclinic fronts ([Grønås and Skeie 1999](#)) and polar lows ([Rasmussen and Turner 2003](#)). Other phenomena related to CAOs are low-level jets (LLJs) in the atmospheric boundary layer (ABL) that have been observed some distance downwind of the ice edge ([Brümmer 1996](#)). Such jets are associated with a significant increase of wind speed in the ABL, exceeding the large-scale geostrophic wind speed by up to 20–30%. A thorough understanding and correct modelling of the LLJ is important since the surface fluxes of heat and momentum are strongly influenced by the LLJ strength over hundreds of kilometres downwind of the marginal sea-ice zone.

The LLJs are not always found in observations or in the results of numerical simulations of CAOs. For instance, idealized numerical simulations and available observations demonstrate that there is a wide range of external forcing parameters for which no LLJ forms ([Chechin et al. 2013](#)).

Although [Chechin et al. \(2013\)](#) showed that the LLJ can be modelled quite well with mesoscale models when the resolution is high enough, results of numerical models alone are not sufficient to really understand the reasons for the LLJ development. However, in [Chechin et al. \(2013, 2015\)](#) it was shown that a mixed-layer model can serve as a good diagnostic tool to study the mixed-layer wind evolution. One can define the strength of the LLJ as the difference between the ABL-averaged wind speed and the large-scale geostrophic wind speed. After that, one can use the mixed-layer assumptions of height-constant temperature and wind-vector components in the ABL to determine the dependence of LLJ strength on the large-scale conditions.

Using a simple mixed-layer model, [Chechin et al. \(2013\)](#) showed that the LLJ strength depends on the baroclinicity in the ABL. The latter, in turn, is governed by the temperature difference between the surface temperatures of sea-ice in the pack-ice region and of open water downstream (see also [Brümmer 1996](#)). They further showed that the ice-edge orientation relative to the direction of the large-scale flow determines the LLJ existence and whether baroclinicity leads to acceleration or deceleration of the flow downwind the ice edge. This finding was confirmed by [Chechin et al. \(2015\)](#) who used mixed-layer assumptions to explain qualitatively the observed spatial variability (maxima and minima) of the 10-m wind speed retrieved from satellite and reanalysis data for CAOs over the Nordic Seas.

In the present paper we aim to obtain more insight into the LLJ development using a mixed-layer model as in [Chechin et al. \(2013, 2015\)](#) that is, however, more complex. The new model describes the mixed-layer potential temperature, height and wind speed as functions of distance from the ice edge. In contrast to the previous work, the new model also accounts for the impact of the inversion slope and processes above the ABL. Using this model we explain the main mechanisms that govern the evolution of wind speed downwind of the ice edge during CAOs.

Our study follows, in principle, the line of earlier studies using a hierarchy of mixed-layer models to investigate different features of CAOs. This includes both analytical and more complex numerical models (e.g., Reynolds 1984; Yuen 1985). The former used linearized mixed-layer equations based on severe idealizations (Yuen and Young 1986); such models are used mainly for qualitative analysis. There is also a class of mixed-layer models (Venkatram 1977; Renfrew and King 2000) that provides a more realistic description of the ABL growth and heating in convective conditions compared to the linearized models and yet can also be solved analytically. The main drawback of the latter class of models, however, is that they neglect the spatial variability of the ABL wind speed and direction. Our new model is a further iteration of the latter class of models. We include equations for the horizontal components of the ABL wind vector and use, for simplicity, the geotriptic (Ekman) balance approximation. Importantly, the improved model is still based on analytical solutions describing the ABL growth and heating.

One might question the necessity to develop a simple mixed-layer model when computational resources today are sufficient to operate large-eddy simulations over large domains spanning hundreds of kilometres (Gryschka et al. 2014). It has also been shown that non-eddy resolving models (Wacker et al. 2005) and modern reanalyses capture the large-scale features of CAOs. Nevertheless, it was stressed by Stevens (2002) that mixed-layer models provide a very useful framework serving several goals: to interpret and organize observations and results from numerical modelling, and to better understand the climatology of the ocean-atmosphere interactions.

In the case of CAOs this interaction is extremely strong and results in the intense cold-air mass transformation over the ocean. Here, we use our mixed-layer model not only to describe the LLJ but also to estimate the typical horizontal scale of the air-mass transformation. This scale has an important climatological meaning as it serves as one of the characteristics of the ocean-atmosphere exchange of heat, momentum and humidity. Moreover, we show that this scale also determines how rapidly the baroclinicity in the ABL decays downwind of the ice edge.

To evaluate the new model we compare its results with measurements made during six days of CAOs over the marginal sea-ice zone in the Fram Strait. The measurements originate from the three aircraft campaigns carried out by the Alfred Wegener Institute (Bremerhaven, Germany). Additionally, observations made by the University of Hamburg (Germany) (Brümmer 1996, 1997) are used. We also perform a detailed comparison of the mixed-layer model results with those of idealized simulations of CAOs using the 3D non-hydrostatic (NH3D) model. The latter was shown (Chechin et al. 2013) to adequately reproduce observed CAOs.

The structure of the paper is as follows: the new mixed-layer model is presented in Sect. 2, and the NH3D model is briefly described in Sect. 3. The results of the mixed-layer model are first compared to observations in the Arctic in Sect. 4 and then with the NH3D model results in Sect. 5. In the Discussion and Conclusions, a horizontal scale of the air-mass transformation is introduced and quantified.

2 Mixed-Layer Model

We present a mixed-layer model that describes the evolution of the ABL-averaged wind speed, potential temperature and the ABL height downwind of the marginal ice zone during Arctic CAOs. A particular focus of the model is on the baroclinicity in the ABL that has a significant impact on the ABL flow.

The mixed-layer model is a steady-state model that consists of: (i) diagnostic momentum equations in the form of geotriptic balance, a balance between the horizontal pressure gradient, Coriolis force and friction; (ii) an equation for potential temperature θ_m ; (iii) an equation for the ABL height z_i ; (iv) an equation for the temperature jump $\Delta\theta$ at the ABL top. Venkatram (1977) proposed a quasi-analytical solution of the latter three equations. To that aim, he assumed that the direction of the ABL flow is constant and equal to the direction of the large-scale flow. By doing so, he made the equations for θ_m , z_i and $\Delta\theta$ independent of the momentum equations. The momentum equations in the form of geotriptic balance were also solved analytically by Byun and Arya (1986) for a given geostrophic wind speed and ABL height.

We propose a quasi-analytical solution of the whole system that, to our knowledge, has not yet been done by others. To that aim, we combine both the solutions of Venkatram (1977) and that of Byun and Arya (1986).

2.1 Mixed-Layer Model Equations

Our strategy is to retain the coupling between the momentum equations and the equations for θ_m and z_i and combine the Venkatram (1977), and Byun and Arya (1986) solutions. To that aim, we use the Venkatram solution to obtain analytical formulae describing the evolution of the ABL-mean geostrophic wind speed $|\mathbf{V}_{gm}|$ and z_i downwind of the ice edge. These solutions are then used in the momentum equations, which can be solved for any given $|\mathbf{V}_{gm}|$ and z_i .

We start with several idealizations to simplify a basic set of dry mixed-layer model equations (see, e.g., Overland et al. 1983). Our further idealizations are the assumptions of, (i) steady state, and (ii) geotriptic balance in the ABL. Additionally, we, (iii) neglect entrainment of momentum at the ABL top, and assume (iv) that the ABL height changes only due to entrainment.

Finally, the dry mixed-layer model is reduced to

$$0 = f(v_m - v_{gm}) - \frac{C_D |\mathbf{V}_m|^2 \sin\phi}{z_i}, \quad (1)$$

$$0 = f(u_{gm} - u_m) - \frac{C_D |\mathbf{V}_m|^2 \cos\phi}{z_i}, \quad (2)$$

$$\frac{\partial\theta_m}{\partial y} = \frac{w_e}{v_m z_i} \Delta\theta + \frac{C_H (\theta_w - \theta_m)}{z_i \cos\phi}, \quad (3)$$

$$\frac{\partial z_i}{\partial y} = \frac{w_e}{v_m}, \quad (4)$$

where u_m , v_m and θ_m are the wind-vector components and potential temperature averaged over the ABL height, respectively, u_{gm} and v_{gm} are the components of the geostrophic wind vector averaged over the ABL height, f is the Coriolis parameter, w_e is the entrainment velocity, $\Delta\theta = \theta_+ - \theta_m$ represents a discontinuous jump of potential temperature at the ABL top where θ_+ is potential temperature right above the ABL top, ϕ is the angle between the y -axis and the direction of the ABL-averaged wind vector.

An equation for $\Delta\theta$ that was not considered explicitly by Overland et al. (1983) needs to be added to Eqs. 1–4. It is formulated as (e.g., Eq. 6.10 in Garratt 1992),

$$\frac{\partial\Delta\theta}{\partial y} = \gamma\theta \frac{\partial z_i}{\partial y} - \frac{\partial\theta_m}{\partial y}, \quad (5)$$

where γ_θ is the potential temperature lapse rate above the ABL.

To close the system, several unknown variables need to be parametrized; these are the exchange coefficients C_D , C_H and the entrainment velocity w_e .

The coefficients C_D and C_H are assumed to be spatially constant over open water, and are evaluated using similarity relations generalized for the mixed layer as proposed by [Dear-dorff \(1972\)](#). For the typical conditions during Arctic CAOs ($\theta_w - \theta_m = 20$ K, $|\mathbf{V}_m| = 10 \text{ m s}^{-1}$, $z_i = 1000$ m), we obtain $C_D = 1.3 \times 10^{-3}$ and $C_H = 1.4 \times 10^{-3}$ using the stability functions of [Arya \(1977\)](#), with aerodynamic roughness length z_{0m} calculated using Charnock’s relation and with a roughness length for heat $z_{0h} = 0.1z_{0m}$. In a wide range of conditions observed during CAOs C_D and C_H do not differ by more than about 15 % from the above values.

The entrainment velocity w_e is by definition

$$w_e = -\frac{(\overline{w'\theta'})_{z_i}}{\Delta\theta}, \tag{6}$$

where $(\overline{w'\theta'})_{z_i}$ is the entrainment heat flux. To parametrize the latter we use the assumption

$$(\overline{w'\theta'})_{z_i} = -\beta(\overline{w'\theta'})_s, \tag{7}$$

where $\beta = 0.2$ is a constant entrainment coefficient and $(\overline{w'\theta'})_s$ is the turbulent heat flux at the surface. The assumption (7) is valid in dry convectively-dominated boundary-layer regimes ([Garratt 1992](#)). Nevertheless, in [Gryschka et al. \(2014\)](#) it was shown using large-eddy simulation that even in the presence of clouds the entrainment buoyancy flux scales well with the surface buoyancy flux over the first 150 km downwind of the ice edge. However, entrainment during high-latitude CAOs has not yet been systematically studied.

Another unknown variable is the along-ice-edge component of the geostrophic wind vector u_{gm} . It strongly differs from the large-scale component U_g due to baroclinicity associated with ABL heating and growth ([Chechin et al. 2013](#)). Analytical formulae for the baroclinic components of u_{gm} are derived further in Sect. 2.4 using the Venkatram solutions for θ_m , z_i and $\Delta\theta$ (Eqs. 3, 4 and 5, respectively).

2.2 Momentum Equations

Equations 1, 2 can be solved analytically for u_m and v_m ([Byun and Arya 1986](#); [Andreas et al. 2000](#)). For that purpose we introduce a new coordinate system (x', y') rotating the original coordinate system (x, y) in a way that the x' -axis is aligned with the geostrophic wind vector averaged over the ABL height \mathbf{V}_{gm} . Analytical solutions of the rotated equations are then

$$\frac{u'_m}{|\mathbf{V}_{gm}|} = \frac{-1 + (1 + 4E_m^2)^{1/2}}{2E_m^2}, \tag{8}$$

$$\frac{v'_m}{|\mathbf{V}_{gm}|} = \text{sgn}(f) \frac{[-1 + (1 + 4E_m^2)^{1/2}]^{3/2}}{2\sqrt{2}E_m^2}, \tag{9}$$

where u'_m and v'_m are the ABL-averaged components of the wind vector in the new coordinate system (x', y') ; $|\mathbf{V}_{gm}| = \sqrt{u_{gm}^2 + v_{gm}^2}$ is the geostrophic wind speed averaged over the ABL height; $E_m = C_D|\mathbf{V}_{gm}|/(|f|z_i)$ is the geostrophic Ekman number.

The values of u_m and v_m can be obtained from Eqs. 8–9 by returning to the original coordinate system. However, the ABL wind speed $|\mathbf{V}_m|$ is invariant with respect to rotation of coordinates, and therefore we simply use $|\mathbf{V}_m| = \sqrt{(u'_m)^2 + (v'_m)^2}$.

Thus, using Eqs. 8–9, $|\mathbf{V}_m|$ can be found at any distance from the ice edge if E_m and $|\mathbf{V}_{gm}|$ are known. In further sub-sections we present analytical solutions for z_i and $|\mathbf{V}_{gm}|$ that are necessary to evaluate E_m . Before that, one important assumption has to be made.

Solutions given by Eqs. 8 and 9 show that the angle ϕ is a function of y because both $|\mathbf{V}_{gm}|$ and E_m change with y . However, as shown in [Chechin et al. \(2013\)](#), a change of ϕ due to baroclinicity is almost cancelled by a change resulting from friction. Thus, it can be assumed that $\phi \approx \alpha$, where α is a constant angle between the large-scale geostrophic wind vector and the y -axis. In Eqs. 3 and 4 (in Eq. 4 $v_m = |\mathbf{V}_m|\cos\phi$) we substitute ϕ by α . This makes Eqs. 3 and 4 independent of the momentum equations (Eqs. 1 and 2) and allows them to be solved analytically following [Venkatram \(1977\)](#), as described in the next sub-section.

2.3 Solutions for θ_m and z_i

To obtain analytical solutions for θ_m , z_i and $\Delta\theta$ as functions of y we closely follow [Venkatram \(1977\)](#), see his Chapter 6 for details). First, we solve Eq. 5 for $\Delta\theta$ by combining it with Eqs. 3 and 4. The solution relates $\Delta\theta$ to z_i as (see, e.g., [Garratt 1992](#), Chap. 6)

$$\Delta\theta = \frac{\gamma_\theta \beta z_i}{1 + 2\beta}, \quad (10)$$

noting that this solution does not allow prescribing any other initial value of $\Delta\theta$ apart from $\Delta\theta_0 = \gamma_\theta \beta z_{i0}/(1 + 2\beta)$, where z_{i0} is the ABL height at the inflow. This might be a drawback in the case of CAOs since a strong capping inversion is often present in the inflow profile (e.g., [Lüpkes and Schlünzen 1996](#)). However, Eq. 10 is particularly useful for the main goal of our study as it allows a simple derivation of relations describing the low-level baroclinicity. Moreover, Eq. 10 is a prerequisite for the quasi-analytical solution of the whole system of the mixed-layer model equations. Thus, we leave a more detailed description of the inversion strength for future research and use Eq. 10 for $\Delta\theta$.

Equations 3, 4 and 10 can be combined and solved for z_i to provide a diagnostic relation between z_i and θ_m given by

$$\bar{z}_i = \bar{\theta}_m. \quad (11)$$

The normalized $\bar{\theta}_m$ and \bar{z}_i are

$$\bar{\theta}_m = \frac{\theta_m - \theta'_{ice}}{\theta_w - \theta'_{ice}}, \quad (12a)$$

$$\bar{z}_i = \frac{z_i}{H}, \quad (12b)$$

where $\theta'_{ice} = \theta_{ice} - \gamma_\theta z_{i0}(1 + \beta)/(1 + 2\beta)$ and H represents the asymptotic ABL height at infinite distance from the ice edge,

$$H = \frac{(\theta_w - \theta'_{ice})(1 + 2\beta)}{\gamma_\theta(1 + \beta)}. \quad (13)$$

Substituting Eq. 11 into Eq. 3 [Venkatram \(1977\)](#) obtained an analytical solution of Eq. 3, namely

$$\ln(1 - \bar{\theta}_m) + \bar{\theta}_m = -C_1 \bar{y} + C_2, \quad (14)$$

where $C_1 = (1 + \beta)C_H$, $C_2 = \bar{\theta}_{m,0} + \ln(1 - \bar{\theta}_{m,0})$, $\bar{\theta}_{m,0} = z_{i0}/H$, and \bar{y} is the normalized distance from the ice edge

$$\bar{y} = \frac{y}{\cos\alpha H}. \quad (15)$$

A slightly modified version of the Venkatram solution is presented above. Unlike Venkatram (1977) we allow for the ABL height z_{i0} to be non-zero at $y = 0$, which leads to C_2 being non-zero in Eq. 14. Additionally, Venkatram assumed $\cos \alpha = 1$ in the denominator of \bar{y} as he considered only the case when the large-scale geostrophic vector wind is orthogonal to a coastline (or an ice edge in our case). Also, we modify the definition of the asymptotic ABL height H by including the factor $(1 + 2\beta)/(1 + \beta)$. With $z_{i0} = 0$ and $\cos \alpha = 1$ Eqs. 11 and 14 become identical to Eqs. 44 and 45 in Venkatram (1977).

2.4 Geostrophic Wind Vector

Using the hydrostatic assumption, one can express \mathbf{V}_{gm} according to Chechin et al. (2013) (their Appendix 1) as

$$u_{gm} = U_g + \underbrace{\frac{g\theta_m}{f} \int_{z_{i+}}^Z \left(\theta^{-2} \frac{\partial \theta}{\partial y} \right)_{bc} dz}_{U_{g+}} - \underbrace{\frac{g\Delta\theta}{f\theta_+} \frac{\partial z_i}{\partial y}}_{U_{gi}} + \underbrace{\frac{gz_i}{2f\theta_m} \frac{\partial \theta_m}{\partial y}}_{U_{gt}}, \tag{16}$$

$$v_{gm} = V_g, \tag{17}$$

where Z refers to a height much larger than z_i where the perturbation of the θ field caused by the change of surface characteristics becomes negligible and the x -component of the geostrophic wind vector is approximately equal to its large-scale value U_g . Subscript “bc” in Eq. 16 refers to the baroclinic part of the horizontal gradient of potential temperature. The latter is defined as the difference between the total $\partial\theta/\partial y$ and its component that is needed to maintain U_g constant with height.

Equation 16 shows that the value of u_{gm} consists of a barotropic part U_g and three baroclinic terms: the second term on the right-hand side (r.h.s.) of Eq. 16 U_{g+} represents the effect of baroclinicity above the ABL in the layer $z_{i+} < z < Z$; the third term U_{gi} corresponds to the effect of the sloping inversion at the ABL top; the fourth term U_{gt} is related to the horizontal gradient of θ in the ABL.

Note that in Overland et al. (1983) the term U_{gi} is called barotropic, because within the mixed layer U_{gi} represents a height-constant addition to the x -component of the geostrophic wind vector in the ABL (see Eq. A5 in Chechin et al. 2013). However, in a continuous three-dimensional atmosphere U_{gi} is produced by the horizontal gradient of θ at $z = z_i$ and thus has a baroclinic origin. Therefore, we call U_{gi} a baroclinic term.

2.4.1 Terms U_{gi} and U_{gt}

In our mixed-layer model framework it is possible to relate U_{gt} and U_{gi} to θ_m (see Appendix 1 for details). By doing so we obtain relations similar to Eq. 14 describing the evolution of U_{gt} and U_{gi} as functions of y and of external forcing parameters, namely

$$\ln(\overline{U_{gt}}) - \overline{U_{gt}} + 1 = -C_1 \bar{y} + C_2, \tag{18}$$

$$\ln(-\overline{U_{gi}}) + \overline{U_{gi}} + 1 = -C_1 \bar{y} + C_2, \tag{19}$$

where the normalized $\overline{U_{gt}}$ and $\overline{U_{gi}}$ are

$$\overline{U_{gt}} = \frac{2f\theta_0 \cos\alpha U_{gt}}{g(1 + \beta)C_H(\theta_w - \theta'_{ice})}, \tag{20}$$

$$\overline{U_{gi}} = \frac{f\theta_0 \cos\alpha U_{gi}}{g\beta C_H(\theta_w - \theta'_{ice})}. \tag{21}$$

Moreover, it is easy to show (see Appendix 1) that

$$\frac{U_{gt}}{U_{gi}} = -\frac{(1 + \beta)\theta_+}{2\theta_m\beta} \approx -\frac{1 + \beta}{2\beta}. \quad (22)$$

Equation 22 shows that for $\beta = 0.2$ the ratio $U_{gt}/U_{gi} = -3$; this estimate shows that U_{gt} represents the dominant baroclinic effect on u_{gm} . Nevertheless, U_{gi} has an opposite sign and is not negligible compared to U_{gt} . It can be shown that entrainment leads to a decrease of the absolute value of $U_{gt} + U_{gi}$ reducing the effect of baroclinicity on u_{gm} .

2.4.2 Parametrization for U_{g+}

For idealized CAOs forced by the large-scale barotropic geostrophic wind vector the term U_{g+} represents a steady-state response of the atmosphere above the ABL to processes in the ABL. This term cannot be described explicitly by the mixed-layer model, and so U_{g+} either has to be prescribed based on observations, based on results from a more complete numerical model, or it has to be parametrized (e.g., Lavoie 1972).

Results of the NH3D model presented in Sect. 5 suggest that the same scaling as for U_{gt} and U_{gi} is appropriate for U_{g+} . In this case, the simplest way to proceed is to assume that U_{g+} is proportional to U_{gt} ,

$$U_{g+} = -\kappa U_{gt}, \quad (23)$$

where κ is a constant. The NH3D model results for U_{g+} shown below suggest the use of $\kappa = 0.3$. The minus sign in Eq. 23 shows that U_{g+} reduces the effect of U_{gt} on u_{gm} in the same way as does U_{gi} .

The proposed parametrization can be used to obtain relations similar to Eqs. 18 and 19 describing U_{g+} as a function of y ,

$$\ln(-\overline{U_{g+}}) + \overline{U_{g+}} + 1 = -C_1\bar{y} + C_2, \quad (24)$$

where C_1 , C_2 and \bar{y} are the same as in Eqs. 18 and 19, and $\overline{U_{g+}}$ is

$$\overline{U_{g+}} = \frac{2f\theta_0\cos\alpha U_{g+}}{\kappa g(1 + \beta)C_H(\theta_w - \theta'_{ice})}. \quad (25)$$

2.5 Summary of the Mixed-Layer Model

The solution procedure of the mixed-layer model consisting of Eqs. 1–5 is the following; the first step is to solve Eqs. 14, 18, 19, 24 iteratively by using Newton's method providing values of $\overline{\theta_m}$, $\overline{U_{gt}}$, $\overline{U_{gi}}$ and $\overline{U_{g+}}$, respectively. After that, \bar{z}_i is found using the diagnostic Eq. 11. The next step is to switch to non-normalized variables and to obtain the values of u_{gm} and, consequently, of $|\mathbf{V}_{gm}|$. Finally, E_m is evaluated and used in Eqs. 8 and 9 to obtain $|\mathbf{V}_m| = \sqrt{(u'_m)^2 + (v'_m)^2}$.

The physical processes taken into account in the mixed-layer model and that lead to a dependence of $|\mathbf{V}_m|$ on the distance from the ice edge are the following:

- the surface heating of the ABL and entrainment that produce a thermal wind (terms U_{gt} and U_{gi});
- the response of the geostrophic wind vector above the ABL top to processes in the ABL (term U_{g+});
- the effect of surface friction on the ABL wind vector controlled by the value of the geostrophic Ekman number E_m .

In the mixed-layer model we neglect the latent heating due to condensation in clouds and also the radiative heat sources; there is evidence that these effects are secondary for the ABL development during Arctic CAOs compared to the ABL heating from the sensible heat flux over the ocean (e.g., Brümmer 1996; Renfrew and Moore 1999; Lüpkes et al. 2012) as already discussed also in Chechin et al. (2013) and Renfrew and King (2000). The reason relates to the low sea-surface temperature downwind of the ice edge resulting in a surface latent heat flux being much smaller than the sensible heat flux, with a Bowen ratio as high as 3-5 (Renfrew and Moore 1999). Far downwind of the ice edge and at a higher sea-surface temperature, latent heating in clouds may play a more important role. However, a detailed consideration of clouds and related processes is beyond the scope of this study.

Another process that we neglected is the entrainment of momentum. To take this into account the additional terms $\Delta u w_e / (v_m z_i)$ and $\Delta v w_e / (v_m z_i)$, where $\Delta u = u_+ - u_m$ and $\Delta v = v_+ - v_m$, need to be added in the r.h.s. of Eqs. 1 and 2, respectively. Since these terms have z_i in the denominator, their effect on the mixed-layer wind speed decreases when z_i increases. Therefore, we expect the entrainment of momentum to be important only close to the ice edge where z_i is small. For the same reason, the effect of surface friction on the mixed-layer wind speed becomes negligible far downwind of the ice edge, as demonstrated in Chechin et al. (2015).

Many assumptions have been made to derive the equations of the present mixed-layer model. To draw conclusions on the validity of these assumptions for typical Arctic CAOs we compare the results of the mixed-layer model, first with observations over the Fram Strait and then with the results of the NH3D numerical model. The latter is briefly presented below.

3 The NH3D Model

The NH3D model (Miranda and James 1992) is a mesoscale non-hydrostatic atmospheric model. The basic model equations are formulated using a terrain-following σ -pressure vertical coordinate system (Miller and White 1984). The NH3D model has been used in the past for the simulation of three-dimensional gravity waves generated by orography (Miranda and Valente 1997) and most recently by Chechin et al. (2013) for the simulation of CAOs. A detailed model description is given in Miranda (1991) and Miranda and James (1992). For the present purpose, we apply the model using the same set-up as in Chechin et al. (2013) so that we concentrate here just on those features that are most relevant for the present application.

Here we slightly modify the non-local turbulence closure proposed by Lüpkes and Schlünzen (1996) and that is used in the NH3D model in convective conditions. We do this to account for the entrainment at the ABL top in closer agreement with large-eddy simulation results of Noh et al. (2003). For the modification, we follow Noh et al. (2003) and introduce an explicit term for the entrainment flux in the heat-flux profile,

$$-\overline{w'\theta'} = K_H \left(\frac{\partial \theta}{\partial z} - \gamma_h \right) - \overline{(w'\theta')}_{z_i} \left(\frac{z}{z_i} \right)^n, \quad (26)$$

where $n = 3$, K_H is the eddy diffusivity for heat and is parametrized as in Lüpkes and Schlünzen (1996) by a profile function independent of local gradients, γ_h is the non-local term for which the parametrization of Holtslag and Moeng (1991) is used. The second term in Eq. 26 represents the entrainment flux that is parametrized similarly as in the mixed-layer model: $\overline{(w'\theta')}_{z_i} = -\beta \overline{(w'\theta')}_s$, where $\beta = 0.2$. The ABL height z_i is determined diagnostically using the same method as in Noh et al. (2003, their Sect.3.5).

Note that horizontal rolls, a typical feature of CAOs, belong to subfilter motions both in the NH3D model (as discussed in detail in [Chechin et al. 2013](#)) and in the mixed-layer models. We do not use any special parametrization for rolls. As concluded by [Gryschka et al. \(2014\)](#), forced roll convection during CAOs does not need to be additionally parametrized in coarse-resolution models. In the current study we do not invoke parametrizations of shortwave and longwave radiation, or of cloud microphysical processes in the NH3D model, for the same reason as we neglect them in the mixed-layer model.

To compare the results of the NH3D model with those of the mixed-layer model the former has to be averaged over the ABL depth. Such averaging is straightforward for θ and $|\mathbf{V}_m|$ while it is less evident for the baroclinic terms U_{gt} , U_{gi} and U_{g+} . The procedure of their evaluation from the NH3D model results is described in Appendix 2.

4 Comparison of the Mixed-Layer Model with Observations

Here we present a comparison of the mixed-layer model results with the measurements carried out during several CAOs over the marginal sea-ice zone in the Fram Strait. To that aim, we use dropsonde and aircraft observations obtained from three research campaigns by the Alfred Wegener Institute (Bremerhaven, Germany): the Radiation and Eddy Flux Experiments 1991 [REFLEX I ([Hartmann et al. 1991](#))] and 1993 [REFLEX II ([Kottmeier et al. 1994](#))] and the Arctic Radiation and Turbulence Interaction Study [ARTIST ([Hartmann 1999](#))].

We consider six days with CAOs over the Fram Strait north-west of Svalbard; these are the cases: 14 October 1991 (REFLEX I); 4, 10 and 11 March 1993 (REFLEX II); 4 and 5 April 1998 (ARTIST). They result from only four independent CAOs while on two occasions (4–5 April 1998 during ARTIST and 10–11 March 1993 during REFLEX II) we have subsequent days belonging to the same CAO episodes. Since 24 h passed between these flights the inflow profiles and especially the geostrophic wind speed differed also between these cases. All of these cases are well documented and observations were used previously for analysis and model evaluation by [Lüpkes and Schlünzen \(1996\)](#), [Hartmann et al. \(1997\)](#), [Wacker et al. \(2005\)](#) and [Chechin et al. \(2013\)](#).

For the REFLEX I and II CAOs, θ_m , z_i , U_{gt} and $|\mathbf{V}_m|$ are evaluated from dropsonde observations, where the dropsondes were released every 50–60 km along the flight tracks in off-ice direction parallel to the ABL flow. For the ARTIST cases we use the observations obtained by the two aircraft, Polar 2 and Polar 4, that were flying through the ABL in a saw-tooth pattern ([Wacker et al. 2005](#)). In the latter case, vertical profiles represent the average between the observations during an ascent and a subsequent descent of an aircraft. A typical distance between the profiles during ARTIST is about 10–30 km.

As reported by [Hartmann et al. \(1997\)](#), dropsonde observations of wind speed were not sufficiently accurate at the time of the REFLEX I and II campaigns to resolve ABL features. Another source of uncertainty is the high variability of the wind speed in convective conditions; its variance is $\approx 1.2\text{--}1.6 \text{ m}^2 \text{ s}^{-2}$ in the middle of the ABL for typical polar CAOs ([Gryanik and Hartmann 2002](#)). Thus, for two cases (4 and 10 March 1993) we also use additional aircraft observations made independently by the University of Hamburg ([Brümmer 1996](#)). These observations represent the wind speed at 90-m height averaged over 30–50 km flight legs made in a direction parallel to the ice edge at different downwind distances.

The ABL height z_i is diagnosed manually from θ profiles as the height at which a sharp increase in $\partial\theta/\partial z$ exceeds a specified threshold value (roughly 0.003 Km^{-1}).

Values of U_{gt} are found using the definition in Eq. 16, and to that aim $\partial\theta_m/\partial y$ has to be evaluated. For the REFLEX I and REFLEX II CAOs, we approximate $\partial\theta_m/\partial y$ by $\Delta\theta_m/\Delta y$

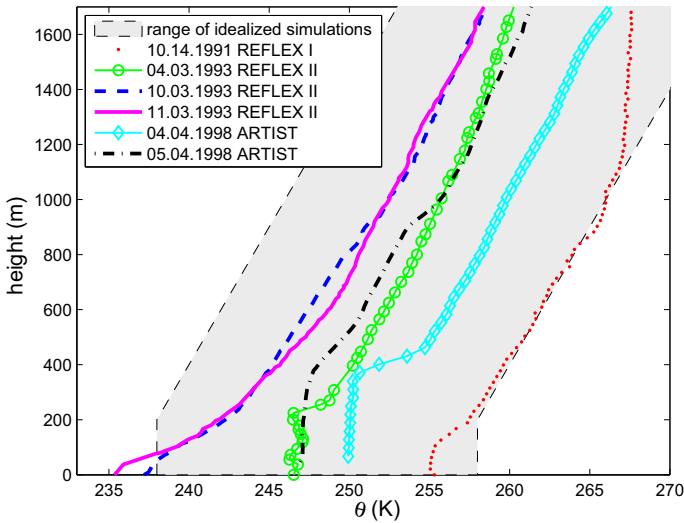


Fig. 1 Vertical profiles of potential temperature observed over the region with compact sea-ice or over the marginal sea-ice zone during six days of CAOs over the Fram Strait. Light grey shading indicates the range of initial profiles used for idealized simulations with the NH3D model

Table 1 Observed values of the mixed-layer model parameters for the six days of CAOs over the Fram Strait

Date	z_{i0} (m)	γ_{θ} (K km ⁻¹)	θ_{ice} (K)	$\theta_w - \theta_{ice}$ (K)	α (°)	$ \mathbf{V}_g $ (m s ⁻¹)
14 October 1991	100	10	255.15	21.5	30	9
4 March 1993	220	9.5	246.8	26.2	33.4	11.3
10 March 1993	0	13.2	237	36	30	6
11 March 1993	40	15.6	234	39	-30	6
4 April 1998	300	11.5	250.5	23.5	0	15.5–17.5
5 April 1998	300	11.5	247	26	0	12.5–15.5

where Δy is the distance along the y -axis between the neighbouring vertical profiles. For the ARTIST CAOs, the distance between the profiles is smaller and, thus, the ABL heating between the neighbouring profiles is smaller. Due to that, the variability of the observed θ_m causes large scatter in the estimates of $\partial\theta_m/\partial y$. To avoid this, $\partial\theta_m/\partial y$ is evaluated as the slope of a linear function approximating the five neighbouring values of θ_m along the y -axis. The linear function is obtained using a least squares fit.

To solve the mixed-layer model for θ_m , z_i and U_{gt} several input parameters have to be prescribed; these are z_{i0} , γ_{θ} , θ_{ice} , $\theta_w - \theta_{ice}$. Their values are obtained from the inflow θ profiles (see Fig. 1) and are summarized in Table 1; the values of γ_{θ} are representative of the lowest 1200–1500 m.

For 4 March 1993 we use the θ profile observed 33 km downwind of the ice edge as an inflow profile. The profile upwind of the ice edge could not be used for that purpose because of a very strong capping inversion. Thus, a single value of γ_{θ} would not be representative for that profile. However, already 33 km downwind, the inversion layer was to a large extent eroded due to ABL heating and entrainment (see Fig. 1 in Chechin et al. 2013 and Fig. 6

in Lüpkes and Schlünzen 1996), and it was much easier to specify γ_θ and other parameters from that profile.

The mixed-layer model requires also a specification of the large-scale geostrophic wind speed $|\mathbf{V}_g|$ and its direction α . The latter parameters are estimated from the inflow profiles of u and v and assumed not to change with y . However, for the ARTIST cases the flow above the ABL strongly increases along the y -axis as demonstrated in Fig. 9 in Wacker et al. (2005). Thus, $|\mathbf{V}_g|$ is prescribed changing linearly from 15.5 m s^{-1} at $y = 0$ to 17.5 m s^{-1} at $y = 250 \text{ km}$ for the CAO on 4 April 1998 and from 12.5 m s^{-1} at $y = 0$ to 15.5 m s^{-1} at $y = 250 \text{ km}$ for the CAO on 5 April 1998.

Figure 2 shows the observed θ_m , z_i and U_{gt} and their normalized values $\overline{\theta_m}$, $\overline{z_i}$ and $\overline{U_{gt}}$ for all the six days of observations. The normalized values together with the mixed-layer solutions given by Eqs. 11, 14 and 18 are plotted against the normalized downstream distance from the ice edge $\hat{y} = C_1\bar{y} - C_2$. It is convenient to use normalized axes because then the mixed-layer model solutions are represented by a single curve for each predicted quantity independent of the choice of input parameters such as $\theta_w - \theta_{ice}$ or γ_θ (see a full list of input parameters in Table 1). The same holds for the observations that should also collapse onto one curve for each quantity as a function of \hat{y} , if the mixed-layer model describes the dominating processes sufficiently realistically.

The observed θ_m curves show a large scatter and vary by up to 20 K; after normalization, $\overline{\theta_m}$ values collapse well onto a single curve. However, the observed values of $\overline{\theta_m}$ are about 10–15 % higher than those obtained from the mixed-layer model solution. Compared to θ_m , the observed z_i has a smaller scatter that is only slightly reduced by normalization. The observed $\overline{z_i}$ is about 20 % smaller than the mixed-layer model solution over the first 100–150 km. Apart from that, Fig. 2 demonstrates a good skill of the mixed-layer model to describe the observed heating and growth of the ABL.

Latent heat release in clouds may be one reason for the underestimation of $\overline{\theta_m}$ by the mixed-layer model. However, subsidence might be another reason that could also explain why the observed $\overline{z_i}$ is smaller than that from the analytical solution. According to Eq. 3, smaller z_i leads to larger $\partial\theta_m/\partial y$, i.e. more rapid heating. Since the underestimation of $\overline{\theta_m}$ is relatively small, we can conclude that the sum of the latent heat release in clouds and of the warming effect by subsidence plays a secondary role for the ABL development compared to the effect caused by sensible heating from the surface and entrainment through the capping inversion. This important conclusion holds for the region considered here, which is relatively close to the ice edge. However, the situation might change further downstream.

The observed values of U_{gt} show large scatter and vary in the range from 3 to about 14 m s^{-1} ; such magnitudes are of the same order as the large-scale geostrophic wind speed. The scatter is much reduced for $\overline{U_{gt}}$ and Fig. 2 demonstrates a reasonable agreement between the mixed-layer model solution and the observations. The observed $\overline{U_{gt}}$ deviate from the analytical solution by up to $\pm 30\%$, and may be partly due to the fact that $\partial\theta_m/\partial y$ is very sensitive to the variability of the instantaneous values of θ_m observed in the convective ABL.

Figure 3 shows the observed and modeled ABL wind speed $|\mathbf{V}_m|$ together with the large-scale geostrophic wind speed derived from the dropsonde measurements above the ABL. Two analytical solutions of the mixed-layer model are presented for each CAO: one obtained with U_{g+} set to zero and another one with U_{g+} parametrized using Eq. 23 with $K = 0.3$.

First of all, Fig. 3 shows that on the three days (4, 10 March 1993 and 14 October 1991) the model qualitatively reproduces the observed LLJ, i.e., that $|\mathbf{V}_m|$ exceeds the large-scale geostrophic wind speed. The model solutions reproduce also the observed wind-speed behaviour on 11 March, on which day the absolute ABL wind speeds are smaller than the large-scale geostrophic wind speed. The absolute values of the modelled wind speed

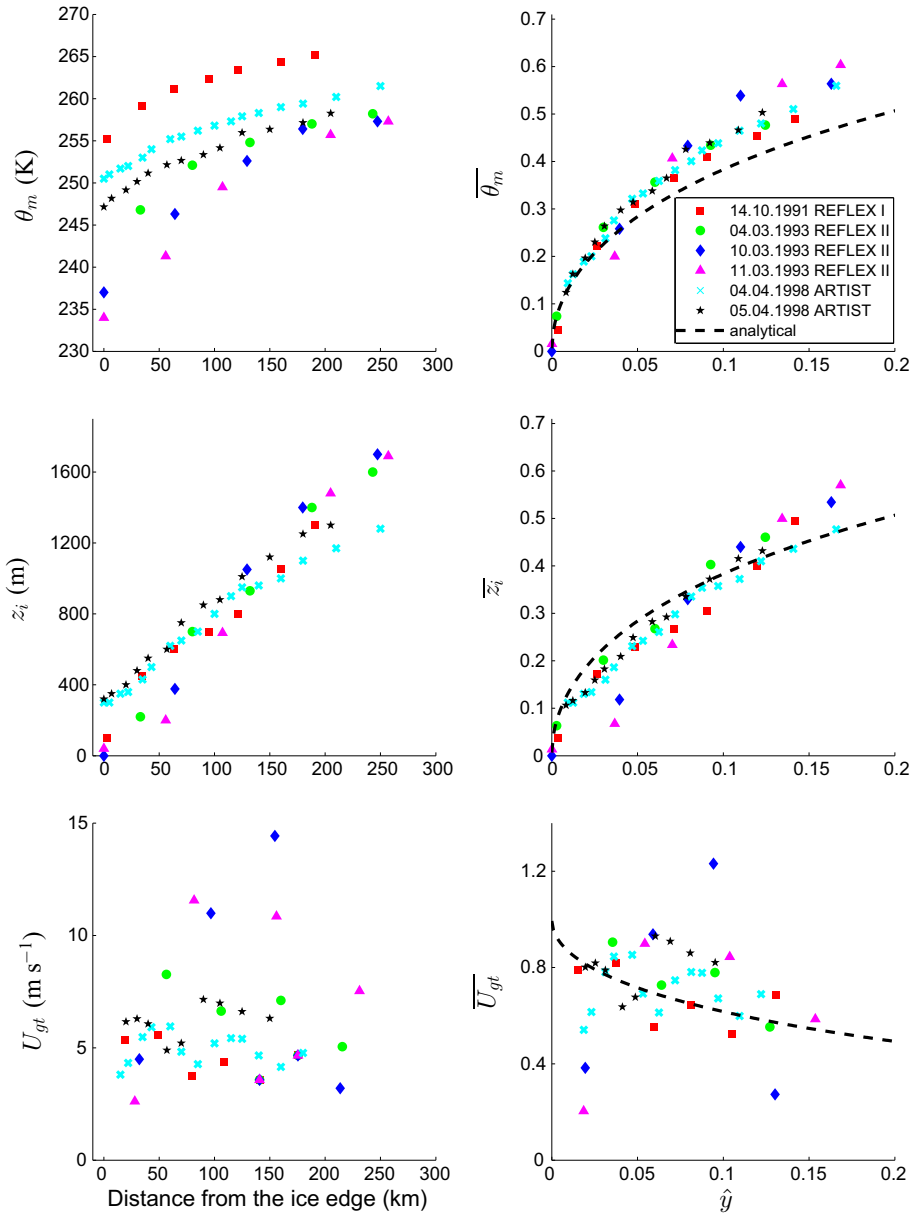


Fig. 2 The observed θ_m , z_i and U_{gt} as functions of distance from the ice edge y (left panel) and their normalized values $\overline{\theta}_m$, \overline{z}_i , \overline{U}_{gt} , with the mixed-layer model solutions (dashed lines) as functions of the normalized distance from the ice edge \hat{y} (right panel) for six CAO days over the Fram Strait

differ between the solutions and they differ also from the observations. However, also the observations by Brümmer (1996) and REFLEX show differences (about 3 m s^{-1}) between each other that are even larger than the difference between observations and model results (about 2 m s^{-1}). So, it is difficult to conclude from this comparison if the parametrized U_{g+}

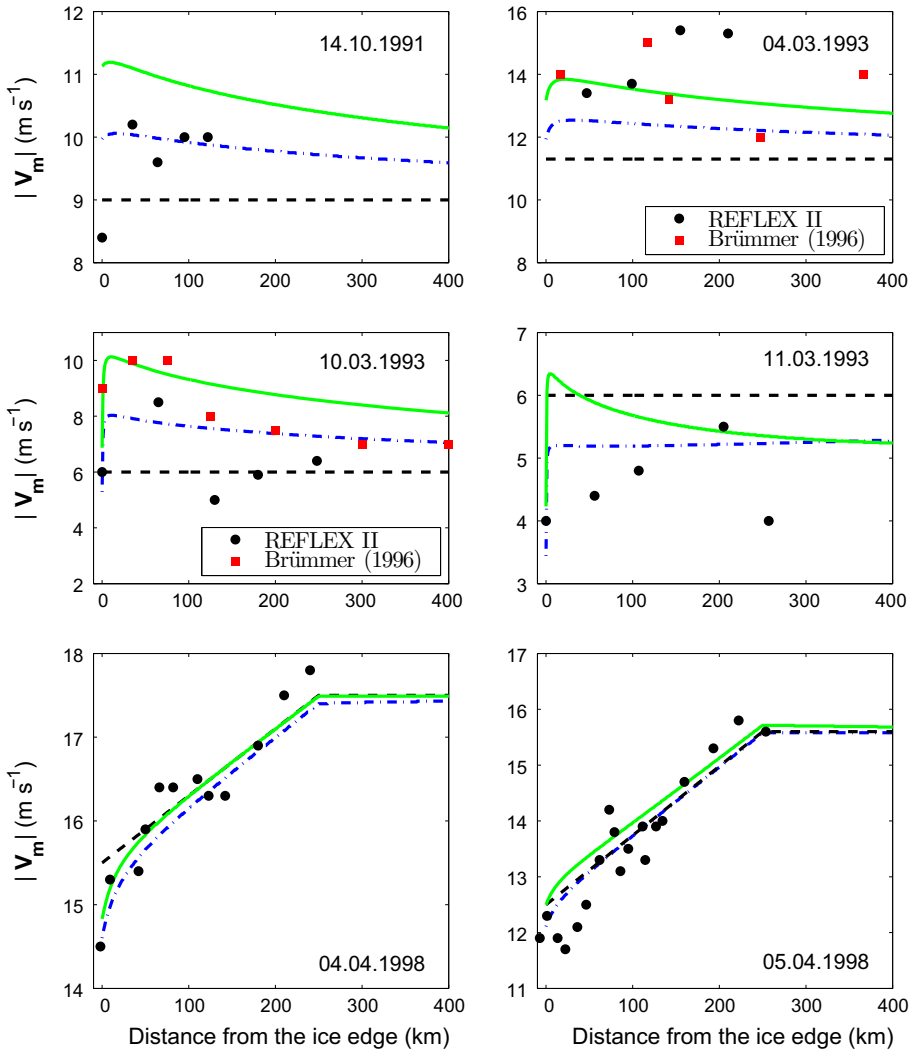


Fig. 3 Wind speed averaged over the ABL height $|V_m|$ from observations and from the mixed-layer model solutions using $U_{g+} = 0$ (green solid line) and parametrization for U_{g+} given by Eq. 23 (blue dot-dashed line). Black dashed line shows the large-scale geostrophic wind speed $|V_g|$ prescribed in the mixed-layer model

improves the model skill. It seems that on 14 October 1991 and on 10 and 11 March 1993 the model version with the new parametrization of U_{g+} agrees better with the observations while it is worse on 4 March 1993.

A very good agreement with the observations is found for both model results on 4-5 April 1998. The difference between the ABL wind speed and the large-scale wind speed does not exceed 1 m s^{-1} (less than 10% of the large-scale wind speed) and no LLJ can be identified both in the observations and in the mixed-layer model results.

This observed behaviour of the ABL wind speed and principle difference between the cases of 4–5 April and data from other days is in agreement with the conclusions of [Chechin](#)

et al. (2013) and can be explained by the sensitivity of the LLJ strength to external parameters. Namely, for moderate $|\mathbf{V}_g|$ not exceeding 15 m s^{-1} the impact of baroclinicity on the ABL wind speed leads to the formation of a LLJ; the LLJ is expected based on Chechin et al. (2013) also for $\alpha > 0$ and large $\theta_w - \theta_{ice}$; for $\alpha < 0$ there should be deceleration of the ABL flow. This sensitivity to external parameters is also well reproduced by the mixed-layer model.

It is not possible to evaluate U_{g+} and U_{gi} from the available observations. Therefore, in the next section we present a comparison of the mixed-layer model results with those of the NH3D model.

5 Comparison with Results from the Non-Hydrostatic Model

It was shown already by Chechin et al. (2013), using the NH3D model, that the strength of the LLJ is especially sensitive to the values of three external parameters. These are (i) the difference between surface temperatures of open water and sea ice ($\theta_w - \theta_{ice}$), (ii) the angle between \mathbf{V}_g and the direction orthogonal to the ice edge (α), and (iii) the large-scale geostrophic wind speed ($|\mathbf{V}_g|$). The performance of the mixed-layer model is explored in a wide range of these parameters, similar to how it was done in Chechin et al. (2013). Namely: $\theta_w - \theta_{ice}$ is varied from 15 to 35 K, α is varied from -45° to 45° , while $|\mathbf{V}_g|$ is varied from 5 to 14 m s^{-1} .

Only the results for various $\theta_w - \theta_{ice}$ and α are considered in detail. This is because we found a very small sensitivity of θ_m, z_i and the baroclinic part of u_{gm} to $|\mathbf{V}_g|$. The mixed-layer model also does not contain $|\mathbf{V}_g|$ as a parameter in the solutions for θ_m, z_i and baroclinic terms in Eq. 16. Only in the solution for $|\mathbf{V}_m|$ does the large-scale geostrophic wind speed occur as a parameter. Therefore, we discuss only the sensitivity of the simulated $|\mathbf{V}_m|$ to $|\mathbf{V}_g|$.

As in the previous section, the results of the NH3D and the mixed-layer models are presented using the normalized variables \bar{z}_i and $\bar{\theta}_m$ (see Eq. 12) as functions of the normalized downstream distance from the ice edge $\hat{y} = C_1 \bar{y} - C_2$.

As described in Appendix 2, based on the output of the NH3D model it is possible to evaluate only $U_{gt} + U_{gi}$ and U_{g+} , but not U_{gt} and U_{gi} separately. Nevertheless, Eq. 22 suggests that U_{gt} and U_{gi} are proportional. Therefore, we also normalize the values of $U_{gt} + U_{gi}$ simulated by the NH3D model in order to plot them as functions of $\hat{y} = C_1 \bar{y} - C_2$. For this purpose we use Eqs. 35 and 22 to obtain

$$\bar{\theta}_m \approx 1 - \frac{2f\theta_0 \cos\alpha}{g(1-\beta)C_H(\theta_w - \theta'_{ice})} (U_{gt} + U_{gi}) \equiv 1 - \overline{U_{gt} + U_{gi}}. \quad (27)$$

Then, we use the latter expression in Eq. 14 and obtain

$$\ln(\overline{U_{gt} + U_{gi}}) - \overline{U_{gt} + U_{gi}} + 1 = -\hat{y}. \quad (28)$$

5.1 Set-up of the NH3D Model Experiments

The set-up of experiments is similar to the one used in Chechin et al. (2013). In the northern part of the NH3D model domain 100% ice cover is assumed with a constant surface temperature θ_{ice} . For the roughness length for momentum $z_{0m} = 0.001 \text{ m}$ is used over sea ice. In the southern part of the domain an ice-free ocean is assumed with a surface temperature at the freezing point $\theta_w = 271.35 \text{ K}$. The roughness length over open water is calculated using Charnock's formula so that $z_{0m} = 0.0185u_*^2/g$. The roughness length for heat is set

to $z_{0h} = 0.1z_{0m}$. The transition between the sea-ice and open water is described by a step change of the sea-ice concentration from 1 to 0. This implies a narrow marginal ice zone as was discussed in detail in Chechin et al. (2013).

The NH3D model is initialized with a vertical temperature profile similar to that measured over sea-ice as shown in Fig. 1. It consists of a well-mixed layer up to the height of 200 m. For $z < 200$ m, $\theta = \theta_{ice}$. For $z > 200$ m, θ grows with height according to $\partial\theta/\partial z = 0.01 \text{ Km}^{-1}$. For experiments with different $\theta_w - \theta_{ice}$ we vary θ_{ice} from 236.35 to 256.35 while keeping $\theta_w = 271.35 \text{ K}$.

The model is forced by a constant in time and space large-scale geostrophic wind vector. In the experiments with different values of $\theta_w - \theta_{ice}$ the components of the large-scale geostrophic wind vector are set to $U_g = 6.2 \text{ m s}^{-1}$ and $V_g = 9.4 \text{ m s}^{-1}$ as observed over the Fram Strait upwind of the ice edge on 4 March 1993. This results in $|\mathbf{V}_g| = 11.26 \text{ m s}^{-1}$ and $\alpha = 33.4^\circ$ corresponding to the north-eastern wind direction. For such a direction a LLJ is expected to form over water (Chechin et al. 2013). In experiments with various α the value of $|\mathbf{V}_g|$ is fixed to 11.26 m s^{-1} .

The computational domain consists of 360 points in the north-south direction with 120 points over the sea-ice. In the east-west direction only six grid points are used. The horizontal grid spacing amounts to 5 km. The vertical grid has 47 levels with a vertical grid spacing increasing from about 30 m close to the ground to about 100 m at 1 km.

The model is run for a 60-h simulation time to ensure that a steady state is established.

5.2 Sensitivity of Results to $\theta_w - \theta_{ice}$

Figure 4 presents the NH3D model results for z_i , θ_m , $U_{gt} + U_{gi}$ and U_{g+} for $\theta_w - \theta_{ice}$ varied from 15 K to 35 K. The left column of Fig. 4 demonstrates that the simulated z_i and θ_m are very sensitive to the values of $\theta_w - \theta_{ice}$. The normalized values of \bar{z}_i and $\bar{\theta}_m$ (right column) collapse well in single curves with the analytical solution from the mixed-layer model. The deviations from this solution do not exceed 10% for \bar{z}_i and $\bar{\theta}_m$.

Figure 4 also shows that the values of $U_{gt} + U_{gi}$ simulated by the NH3D model are very sensitive to $\theta_w - \theta_{ice}$ and also collapse onto a single curve with the mixed-layer model solution. For $\bar{U}_{gt} + \bar{U}_{gi}$ more scatter around the analytical solution is obtained being largest close to the ice edge where the deviation is as high as about $\pm 20\%$.

Figure 4 contains also curves for U_{g+} produced by the NH3D model. It can be seen that U_{g+} is of opposite sign compared to $U_{gt} + U_{gi}$ and is about a factor of two smaller than $U_{gt} + U_{gi}$. The values of U_{g+} are very sensitive to $\theta_w - \theta_{ice}$, but after we normalize U_{g+} according to Eq. 25 with $\kappa = 0.3$, the scatter of \bar{U}_{g+} is much reduced. As seen from Fig. 4 the parametrization for U_{g+} (Eq. 23) is not valid close to the ice edge but describes well the large-scale decay of $|U_{g+}|$. Far from the ice edge the scatter of \bar{U}_{g+} around the analytical solution amounts up to about $\pm 25\%$.

Figure 5 shows the values of $|\mathbf{V}_m| - |\mathbf{V}_g|$ simulated by the NH3D and mixed-layer models. Both models produce an acceleration of the flow in the ABL in close agreement with each other. In both models the LLJ strength is proportional to $\theta_w - \theta_{ice}$ and also $|\mathbf{V}_m| - |\mathbf{V}_g|$ slowly decays downwind from the location of the maximum. Such good agreement is partly due to the new parametrization of U_{g+} (Eq. 23). When U_{g+} is set to zero the mixed-layer model overestimates $|\mathbf{V}_m| - |\mathbf{V}_g|$ by about factor of two (not shown here).

The mixed-layer model produces the wind-speed maximum closer to the ice edge (at about 50 km) than the NH3D model (at about 70–150 km). This can be explained by the fact that in the mixed-layer model we neglect the horizontal advection of momentum and also the

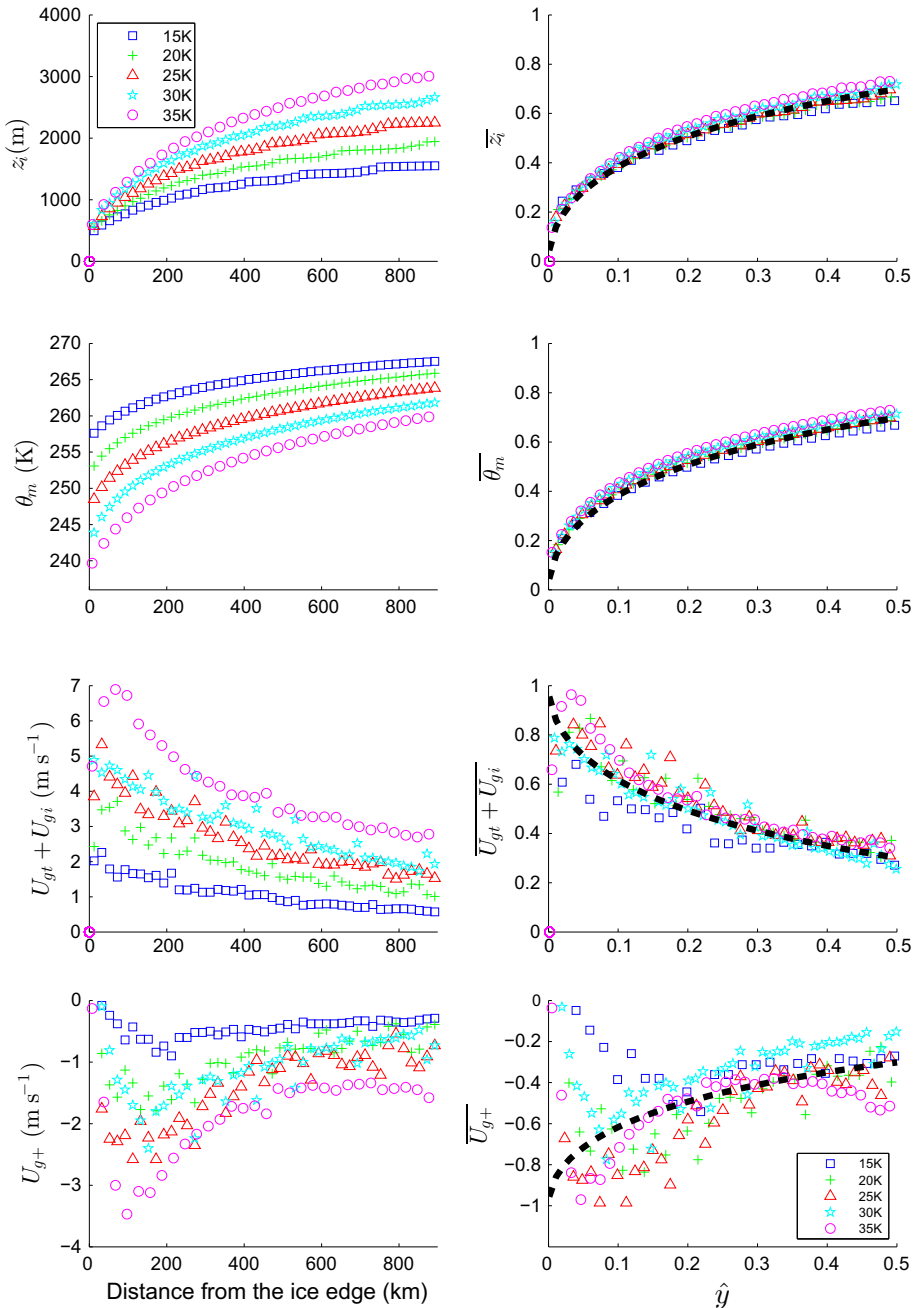


Fig. 4 The ABL height z_i , potential temperature averaged over the ABL depth θ_m , the baroclinic components of the geostrophic wind vector in the ABL $U_{gt} + U_{gi}$ and U_{g+} , as simulated by the NH3D model (left panels) and their normalized values (see Eqs. 12, 25 and 27 for normalizations) and solutions of the mixed-layer model (right panels) for $\theta_w - \theta_{ice}$ varied from 15 to 35 K. The dashed line represents solutions of the mixed-layer model

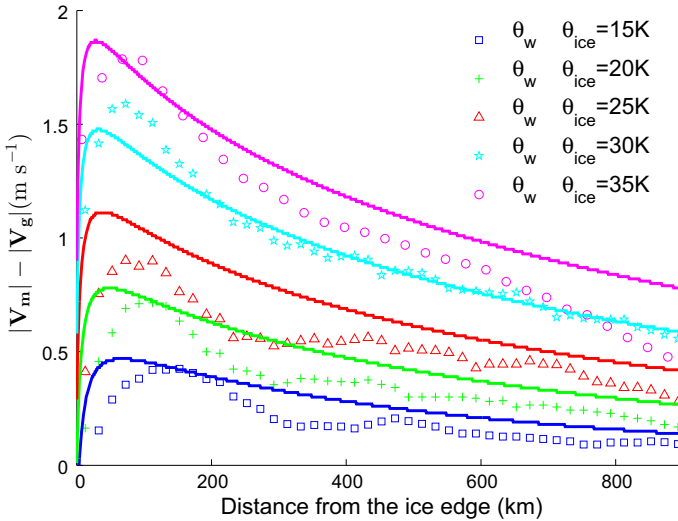


Fig. 5 The difference between the wind speed averaged over the ABL depth and the large-scale geostrophic wind speed $|V_m| - |V_g|$ as simulated by the NH3D and mixed-layer (*solid lines*) models for $\theta_w - \theta_{ice}$ varied from 15 to 35 K

entrainment of momentum. Both of these factors reduce the acceleration of the flow close to the ice edge in the NH3D model.

It is interesting to note that $|V_m| - |V_g|$ produced by the NH3D model demonstrates a non-linear sensitivity to $\theta_w - \theta_{ice}$. This can be seen in Fig. 5 especially by comparing the distance between the red and cyan curves for the mixed-layer and the NH3D models. In contrast to the mixed-layer model results the NH3D model results show increased wind speed differences from the red to the cyan curve. It is hard to give any physical interpretation to this effect in the NH3D model, and may be due to a numerical artefact. However, the magnitude of this effect is not large.

5.3 Sensitivity of the Results to α and $|V_g|$

Figure 6 shows a good agreement between the results of the two models with respect to z_i , θ_m , $U_{gt} + U_{gi}$ for different α . Deviations of the mixed-layer model results from those of the NH3D model do not exceed about 10–15%. It can also be seen that the sensitivity to α is not as large as for $\theta_w - \theta_{ice}$.

Figure 6 shows further that U_{g+} is of opposite sign compared to $U_{gt} + U_{gi}$ for all values of α . The absolute values of U_{g+} are smaller than those of $U_{gt} + U_{gi}$ by roughly a factor of two. After normalization the scatter of $\overline{U_{g+}}$ reduces very slightly. The values of $\overline{U_{g+}}$ differ by up to 50% from the analytical solution given by Eq. 24. This demonstrates that the process of adjustment of the atmosphere above the ABL to the ABL modification is rather complex and cannot be captured by a simple parametrization given by Eq. 23. Nevertheless, we recommend Eq. 23 as it significantly reduces the disagreement between the results of the NH3D and the mixed-layer models with respect to u_{gm} and $|V_m|$.

Figure 7 shows $|V_m| - |V_g|$ as produced by the NH3D and the mixed-layer models for various α and $|V_g|$, and demonstrates a good agreement between the results of the two models. However, it can be seen that the NH3D model produces a more pronounced maximum close

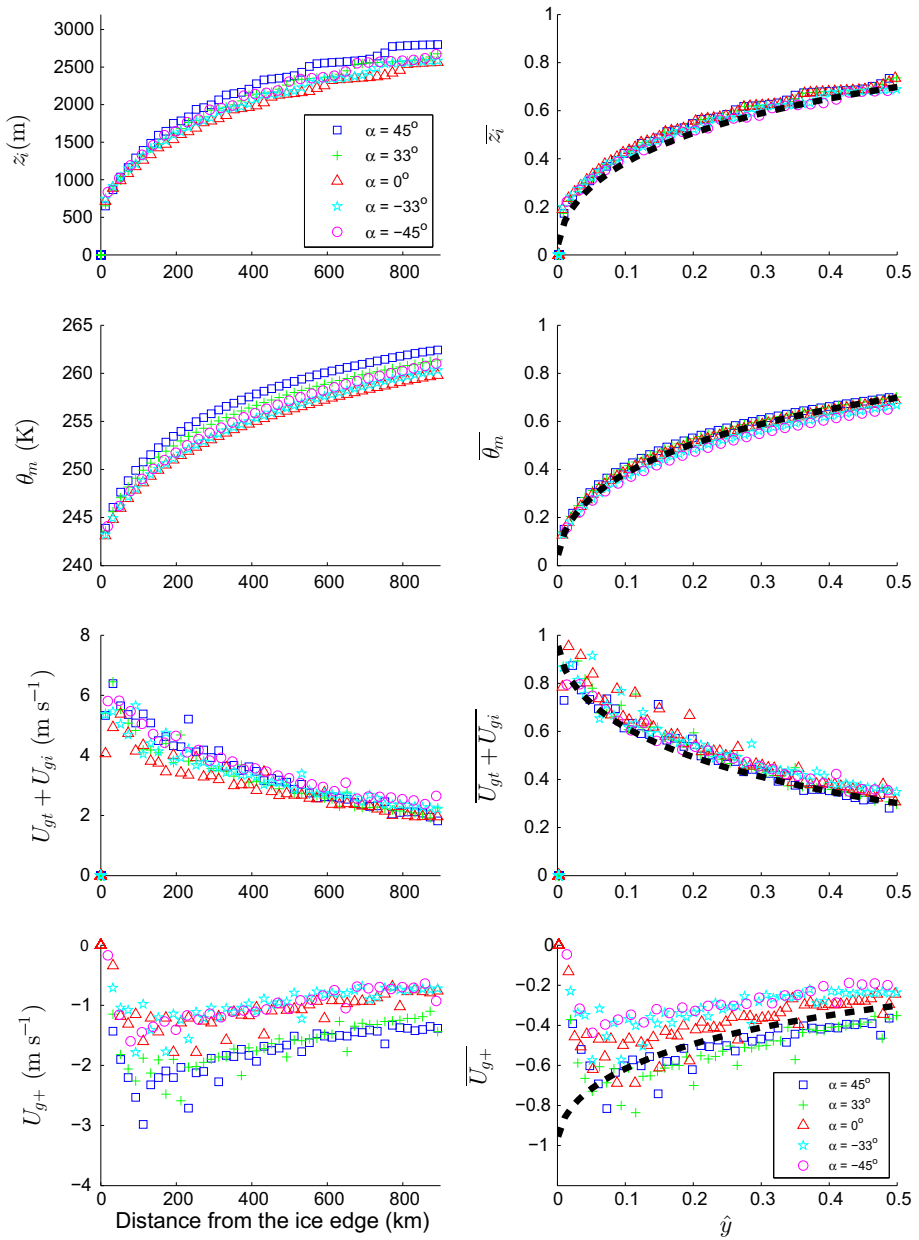


Fig. 6 Same as in Fig. 4 but for α varied from -45° to 45°

to the ice edge, especially for $\alpha = 0$, which is not captured by the mixed-layer model. As discussed in Savijärvi (2011), and Yuen and Young (1986), such a mesoscale maximum can be related to inertial oscillations. In the mixed-layer model inertial oscillations are filtered out because of the neglect of horizontal advection of momentum.

It is clearly seen from Fig. 7 that for negative α both models produce a deceleration of the flow in the ABL, while for positive α the acceleration of similar magnitude is obtained. This

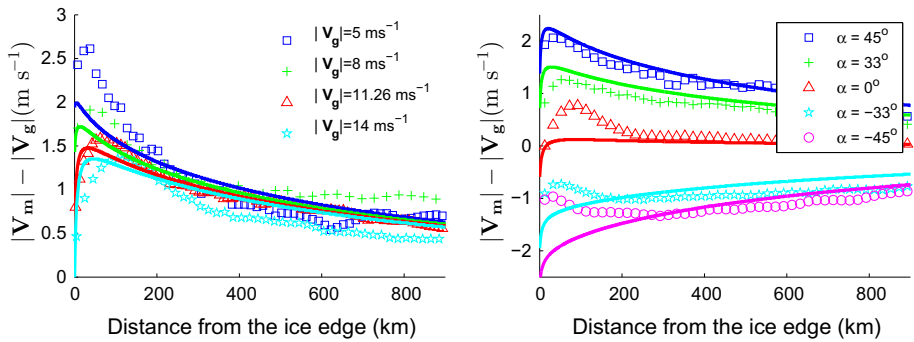


Fig. 7 The difference between the wind speed averaged over the ABL depth and the large-scale geostrophic wind speed $|\mathbf{V}_m| - |\mathbf{V}_g|$ as simulated by the NH3D and the mixed-layer (solid lines) models for α varied from -45° to 45° and for $|\mathbf{V}_g|$ varied from 5 m s^{-1} to 14 m s^{-1}

is explained by the fact that U_{gt} is positive while U_g is negative for $\alpha < 0$. This results in a decrease of $|\mathbf{V}_{gm}|$ and $|\mathbf{V}_m|$, as has been discussed in Chechin et al. (2013).

Figure 7 also demonstrates that $|\mathbf{V}_m| - |\mathbf{V}_g|$ is larger for smaller $|\mathbf{V}_g|$ close to the ice edge, especially in the NH3D model results. Two factors can lead to this sensitivity. First, larger $|\mathbf{V}_g|$ means larger horizontal advection of momentum which is reducing acceleration. Second, larger $|\mathbf{V}_g|$ leads to larger E_m and, thus, stronger deceleration due to friction (see Eqs. 8 and 9). Only the latter effect is taken into account in the mixed-layer model and this explains the smaller sensitivity of $|\mathbf{V}_m| - |\mathbf{V}_g|$ to $|\mathbf{V}_g|$ in the mixed-layer model.

6 Discussion and Conclusions

It is shown that the mixed-layer model describes well the ABL heating and growth during Arctic CAOs. This is demonstrated both by the comparison with observations over the Fram Strait and also with results of the non-hydrostatic NH3D model. The analytical solutions underestimate the mixed-layer potential temperature by about 10–15% compared to observations, which could be due to the neglect of the latent heat release in clouds and subsidence. Still, a good agreement with observations confirms earlier results that these factors play a secondary role for the ABL development during Arctic CAOs over the first about 250 km downwind the marginal ice zone.

The observed baroclinicity related with the ABL heating (term U_{gt}) is also well reproduced by the mixed-layer model. The magnitude of U_{gt} is as large as 10 m s^{-1} over the first 200 km downwind the ice edge for some of the observed CAOs. This is comparable with the magnitude of the large-scale geostrophic wind speed. The other two baroclinic terms, U_{gt} and U_{g+} , where the latter represents baroclinicity above the ABL, are smaller and of opposite sign reducing the effect of U_{gt} on the mixed-layer wind speed. The NH3D model simulations allow the quantification of U_{g+} and show that it can be well approximated as a fraction of U_{gt} . Using this as a parametrization for U_{g+} in the mixed-layer model it is possible to obtain a good agreement between results of the two models with respect to the mixed-layer wind speed.

Our results suggest that baroclinicity is the main reason for the observed departure of the mixed-layer wind speed from the large-scale geostrophic wind speed. This conclusion is further supported by the ability of the mixed-layer model to predict whether deceleration or acceleration of the ABL flow is present in the observations or in the NH3D model results.

The presented mixed-layer model is applicable both in the Arctic and Antarctic, as well as in mid-latitudes. However, in the latter case, one should use the parametrization for U_{g+} with care since it is based on results of the NH3D model for the latitude 80° North.

Since the mixed-layer model is shown to reproduce well the ABL modification, it can be used to estimate the horizontal scale of the cold-air mass transformation L_{tr} . This scale serves for a quantification of the region influenced by CAOs. After Guest et al. (1995), we define L_{tr} as the distance at which $(1 - \bar{\theta}_m)$ becomes e times smaller than its value at the ice edge. Equation 14 is used to provide a direct estimate of L_{tr} . This is done by substituting $\bar{\theta}_m = 1 - (1 - \bar{\theta}_{m,0})/e$ and $C_2 = \ln(1 - \bar{\theta}_{m,0}) + \bar{\theta}_{m,0}$ in Eq. 14 where $\bar{\theta}_{m,0} = z_{i0}/H$ is the value of $\bar{\theta}_m$ for $\bar{y} = 0$. This results in

$$L_{tr} = \frac{\cos\alpha}{eC_H(1 + \beta)} [(e - 1)z_{i0} + H], \quad (29)$$

nothing that this represents a refinement of the expressions for L_{tr} by Guest et al. (1995) and Yuen and Young (1986). Guest et al. obtained $L_{tr} = h/C_H$, where h is a constant typical value of the ABL height downwind the ice edge. Their expression is based on the assumptions $\alpha = 0$, $\beta = 0$ and $z_i = h$ applied to the heat conservation Eq. 3 (see Eq. 1 in Guest et al. 1995). Yuen and Young allowed entrainment at the ABL top ($\beta > 0$) and also $\alpha \neq 0$ to obtain $L_{tr} = h\cos\alpha/[(1 + \beta)C_H]$ (their Eq. 24).

The advantages of the length scale described here (Eq. 29) are that, (i) the growth of the ABL is taken into account, and (ii) the value of H is not chosen arbitrarily but is determined by external parameters. Therefore, we examine Eq. 29 in the following in more detail. It shows that the variability of L_{tr} is primarily governed by the parameters $\theta_w - \theta_{ice}$, z_{i0} , γ_θ and $\cos\alpha$. However, Eq. 29 clearly shows that L_{tr} depends explicitly neither on the absolute value of geostrophic wind $|\mathbf{V}_g|$ nor on the mixed-layer wind $|\mathbf{V}_m|$. Therefore, we obtain the remarkable result that although the surface fluxes of heat and momentum strongly depend on wind speed this has almost no effect on the ABL heating and growth.

For the parameter values used in this study ($\beta = 0.2$; $C_H = 1.4 \times 10^{-3}$; $z_{i0} = 200$ m; $\gamma_\theta = 0.01$ K m $^{-1}$; $\alpha = 33^\circ$) L_{tr} varies between 423 km and 855 km while $\theta_w - \theta_{ice}$ is varied from 15 K to 35 K. These large values explain why the surface heat fluxes remain very high, even hundreds of kilometres downwind of the ice edge (e.g., Wacker et al. 2005).

Guest et al. estimated the typical L_{tr} in the Fram Strait and the Barents Sea in spring during off-ice flow to 300 km using $h = 500$ m and $C_H = 1.5 \times 10^{-3}$. Such value for L_{tr} is significantly smaller than our estimates. The same horizontal scale L_{tr} describes the decay of U_{gt} and U_{gi} downstream the ice edge. This follows from Eqs. 18 and 19. This means that for larger $\theta_w - \theta_{ice}$ the low-level baroclinicity decays over a larger distance downstream the ice edge. Thus, for positive α a LLJ can exist over larger ocean areas that leads in turn to increased fluxes of heat and momentum.

It is important to note that the horizontal scale L_{tr} defined here is different from the horizontal scale of the ice-breeze jet L introduced in Chechin et al. (2013). The latter corresponds to the horizontal width of the wind-speed maximum close to the ice edge and is several times smaller than L_{tr} . The scale L in Chechin et al. (2013) serves to describe mesoscale processes of the inertial-gravitational nature close to the ice edge while L_{tr} corresponds to the large-scale air-mass modification.

Summarizing, it is demonstrated that the evolution of the convective ABL and the horizontal variability of wind speed in high-latitude CAOs can be well described by a mixed-layer model when the dominating physical mechanisms are included. This shows also the ability of such models to identify these mechanisms. The description of the mixed-layer parameters as functions of distance downwind the ice edge, as provided by the mixed-layer model, might

also be useful in studies of such phenomena associated with CAOs as polar lows, low-level fronts, convective rolls and cells.

Acknowledgements The authors thank Vladimir Gryanik for many inspiring ideas and critical comments on the topic of the paper, Jörg Hartmann for processing the aircraft measurements and Josh Studholme for improving the language. The work is funded by Grants of the Russian Foundation for Basic Research 14-05-00959, 13-05-41443, 14-05-00038, 14-05-91752 and the Russian Federation President Grant MK-7200.2015.5. That part of the work concerning the air-mass transformation process was funded by the Russian Science Foundation Grant 14-17-00647. The NH3D model experiments were supported by the Supercomputing Center of the Lomonosov Moscow State University. We also gratefully acknowledge the support by the SFB/TR172 "Arctic Amplification: Climate Relevant Atmospheric and Surface Processes, and Feedback Mechanisms (AC)³" in Project A03 funded by the Deutsche Forschungsgemeinschaft (DFG).

Appendix 1 Terms U_{gt} and U_{gi}

Terms U_{gt} and U_{gi} according to Eq. 16 are

$$U_{gt} = \frac{gz_i}{2f\theta_m} \frac{\partial\theta_m}{\partial y}, \quad (30)$$

$$U_{gi} = -\frac{g\Delta\theta}{f\theta_+} \frac{\partial z_i}{\partial y}. \quad (31)$$

In Eq. 30 we substitute $\partial\theta_m/\partial y$ using Eq. 3 and parametrization for w_e given by Eqs. 6 and 7 to obtain

$$U_{gt} = \frac{g(1+\beta)C_H(\theta_w - \theta_m)}{2f\theta_m \cos\alpha}. \quad (32)$$

In Eq. 31 we substitute $\partial z_i/\partial y$ using Eq. 4 with parametrization for w_e

$$U_{gi} = -\frac{g\beta C_H(\theta_w - \theta_m)}{f\theta_+ \cos\alpha}. \quad (33)$$

In Eqs. 32 and 33 an assumption $\phi \approx \alpha$ is used. It is straightforward to obtain the fraction U_{gt}/U_{gi} ,

$$\frac{U_{gt}}{U_{gi}} = -\frac{(1+\beta)\theta_+}{2\theta_m\beta} \approx -\frac{1+\beta}{2\beta}. \quad (34)$$

In the denominators of the terms on the right-hand side of Eqs. 32 and 33 we can substitute θ_m and θ_+ by a constant reference value θ_0 that is independent from y . This is justified by the fact that θ_m and θ_+ change over water by less than 10% from their initial values over the ice. This is not the case for $(\theta_w - \theta_m)$ in the nominators in Eqs. 32 and 33, which depends very strongly upon y . After that, both U_{gt} and U_{gi} become linear functions of θ_m .

Now, U_{gt} and U_{gi} can be expressed as functions of $\overline{\theta_m}$. This can be done by a substitution $\theta_w - \theta_m = (\theta_w - \theta'_{ice})(1 - \overline{\theta_m})$ in Eqs. 32 and 33, where $\theta'_{ice} = \theta_{ice} - \gamma_{\theta} z_{i0}(1 + \beta)/(1 + 2\beta)$. After that, we can obtain useful relations similar to Eq. 14 describing the evolution of U_{gt} and U_{gi} as functions of \bar{y} and of external forcing parameters. To that aim, we express $\overline{\theta_m}$ as a function first of U_{gt} and then of U_{gi} .

$$\overline{\theta}_m = 1 - \frac{2f\theta_0\cos\alpha U_{gt}}{g(1+\beta)C_H(\theta_w - \theta'_{ice})} \equiv 1 - \overline{U}_{gt}, \tag{35}$$

$$\overline{\theta}_m = 1 + \frac{f\theta_0\cos\alpha U_{gi}}{g\beta C_H(\theta_w - \theta'_{ice})} \equiv 1 + \overline{U}_{gi}. \tag{36}$$

Then, we use Eqs 35–36 in Eq. 14 and obtain

$$\ln(\overline{U}_{gt}) - \overline{U}_{gt} + 1 = -C_1\bar{y} + C_2, \tag{37}$$

$$\ln(-\overline{U}_{gi}) + \overline{U}_{gi} + 1 = -C_1\bar{y} + C_2. \tag{38}$$

Appendix 2 Geostrophic Wind in the NH3D Model

Here, the calculation of the ABL-mean x -component u_{gm} of the geostrophic wind vector and the baroclinic terms U_{gt} , U_{gi} and U_{g+} is addressed. To obtain them from the NH3D model variables we consider the equation for the v -component of wind vector used in the NH3D model. It is given by

$$\frac{dv}{dt} = -\frac{\partial\phi'}{\partial y} + \frac{\partial\phi'}{\partial\sigma} \frac{\sigma}{p_*} \frac{\partial p_*}{\partial y} + fU_g - fu, \tag{39}$$

where we neglect diffusion as we are interested now only in the u -component of the geostrophic wind. In Eq. 39 $\phi' = \phi - \phi_{ref}$ is the deviation of geopotential from its reference-state value ϕ_{ref} ; $\sigma = (p - p_{top})/p_*$ is the terrain-following vertical coordinate where $p_* = p_{surf} - p_{top}$ is the pressure difference between the surface and the model-top values.

The first three terms on the right-hand side of Eq. 39 represent the horizontal pressure gradient force. In particular, the first two terms are associated with baroclinicity. The third term is the constant in space and time barotropic forcing.

After averaging Eq. 39 over the ABL height one easily obtains the correspondence between the baroclinic terms of the geostrophic wind in the mixed-layer and the NH3D models

$$u_{gm} - U_g = U_{g+} + U_{gi} + U_{gt} = \frac{1}{fz_i} \int_0^{z_i} -\frac{\partial\phi'}{\partial y} + \frac{\partial\phi'}{\partial\sigma} \frac{\sigma}{p_*} \frac{\partial p_*}{\partial y} dz. \tag{40}$$

Note, that Eq. 40 differs from Eq. 16 as the latter is based on several assumptions of the mixed-layer model.

The baroclinic part of the x -component of the geostrophic wind vector right above the inversion height at $z = z_{i+}$ is

$$U_{g+} = -\frac{\partial\phi'}{\partial y} \Big|_{z=z_{i+}} + \frac{\partial\phi'}{\partial\sigma} \frac{\sigma}{p_*} \frac{\partial p_*}{\partial y} \Big|_{z=z_{i+}}. \tag{41}$$

It is not possible to define z_{i+} in the NH3D model exactly as in the mixed-layer model since there it is based on the assumption of an idealized structure of the ABL and its capping inversion. So, we evaluate the terms on the right-hand side of Eq. 41 at height $z = (1 + \delta)z_i$ with $\delta = 0.1$. We found that a variation of δ by $\pm 50\%$ changed the results presented in Sect. 5 only marginally.

It is also impossible to evaluate U_{gi} directly from the results of the NH3D model because one cannot give an exact location and value of the horizontal gradient of geopotential produced by the sloping inversion at the ABL top. However, it is sufficient to evaluate the sum $U_{gt} + U_{gi}$ since we expect U_{gi} to be a fraction of U_{gt} according to Eq. 22 so that $U_{gt}/U_{gi} \approx -(1+\beta)/2\beta$. The sum $U_{gt} + U_{gi}$ is evaluated by subtracting the value of U_{g+} diagnosed using Eq. 41 from the value of $U_{g+} + U_{gi} + U_{gt}$ diagnosed using Eq. 40.

References

- Andreas EL, Claffy KJ, Makshtas AP (2000) Low-level atmospheric jets and inversions over the Western Weddell Sea. *Boundary-Layer Meteorol* 97(3):459–486
- Arya SPS (1977) Suggested revisions to certain boundary layer parameterization schemes used in atmospheric circulation models. *Mon Weather Rev* 105:215–227
- Brümmer B (1996) Boundary layer modification in wintertime cold-air outbreaks from the Arctic sea ice. *Boundary-Layer Meteorol* 80:109–125
- Brümmer B (1997) Boundary layer mass, water and heat budgets in wintertime cold-air outbreaks from the Arctic sea ice. *Mon Weather Rev* 125:1824–1837
- Brümmer B, Pohlmann S (2000) Wintertime roll and cell convection over Greenland and Barents Sea regions: a climatology. *J Geophys Res* 105(D12):15559–15566
- Byun D-W, Arya SPS (1986) A study of mixed-layer momentum evolution. *Atmos Environ* 20(4):715–728
- Chechin DG, Lüpkes C, Repina IA, Gryanik VM (2013) Idealized dry quasi 2-D mesoscale simulations of cold-air outbreaks over the marginal sea ice zone with fine and coarse resolution. *J Geophys Res* 118:8787–8813
- Chechin DG, Zabolotskikh EV, Repina IA, Shapron B (2015) Influence of baroclinicity in the atmospheric boundary layer and Ekman friction on the surface wind speed during cold-air outbreaks in the Arctic. *Izv Atmos Ocean Phys* 51(2):127–137
- Deardorff JW (1972) Parameterization of the planetary boundary layer for use in general circulation model. *Mon Weather Rev* 100:93–106
- Garratt JR (1992) *The atmospheric boundary layer*. Cambridge University Press, Cambridge, UK 316 pp
- Gryschka M, Fricke J, Raasch S (2014) On the impact of forced roll convection on vertical turbulent transport in cold air outbreaks. *J Geophys Res* 119:12513–12532
- Grønas A, Skeie P (1999) A case study of strong winds at an Arctic front. *Tellus* 51:865–879
- Gryanik VM, Hartmann J (2002) A turbulence closure for the convective boundary layer based on a two-scale mass-flux approach. *J Atmos Sci* 59(18):2729–2744
- Guest PS, Davidson KL, Overland JE, Frederickson PA (1995) Atmosphere-ocean interaction in the marginal ice zones of the Nordic Seas. In: Walker O, Grebmeier J (eds) *Arctic oceanography: marginal ice zones and continental shelves*. American Geophysical Union, Washington DC, pp 51–95
- Hartmann J, Kottmeier K, Raasch S (1997) Roll vortices and boundary-layer development during a cold air outbreak. *Boundary-Layer Meteorol* 84(1):44–65
- Hartmann J, Kottmeier K, Wamser C (1992) Radiation and Eddy flux experiment 1991. *Reports Polar Res Bremerhaven* 105:72
- Hartmann J et al (1999) Arctic radiation and turbulence interaction study. *Reports Polar Res Bremerhaven* 305:81
- Holtzlag AAM, Moeng C-H (1991) Eddy diffusivity and countergradient transport in the convective atmospheric boundary layer. *J Atmos Sci* 48(14):1690–1698
- Kottmeier C, Hartmann J, Wamser C, Bocher A, Lüpkes C, Freese D, Cohrs W (1994) Radiation and Eddy flux experiment 1993 (REFLEX II). *Reports Polar Res Bremerhaven* 132:62
- Lavoie RL (1972) A mesoscale numerical model of lake-effect storms. *J Atmos Sci* 29:1025–1040
- Lüpkes C, Schlünzen KH (1996) Modelling the arctic convective boundary-layer with different turbulence parameterizations. *Boundary-Layer Meteorol* 79(1):107–130
- Lüpkes C et al (2012) Mesoscale modelling of the Arctic atmospheric boundary layer and its interaction with sea ice. In: Lemke P, Jacobi H-W (eds) *ARCTIC climate change the ACSYS decade and beyond*. Atmospheric and oceanographic sciences library. Springer, Netherlands, pp 279–324
- Miranda PMA (1991) Gravity waves and wave drag in flow past three-dimensional isolated mountains. Ph.D. dissertation, University of Reading, 191pp. (Available from University of Reading, Reading RG6 2AU, UK)
- Miranda PMA, James IN (1992) Non-linear three-dimensional effects on gravity-wave drag: splitting flow and breaking waves. *Q J R Meteorol Soc* 118(508):1057–1081
- Miranda PMA, Valente MA (1997) Critical level resonance in three-dimensional flow past isolated mountains. *J Atmos Sci* 54(12):1574–1588
- Miller MJ, White AA (1984) On the non-hydrostatic equations in pressure and sigma coordinates. *Q J R Meteorol Soc* 110(464):515–533
- Noh Y, Cheon WG, Hong SY, Raasch S (2003) Improvement of the K-profile model for the planetary boundary layer based on large eddy simulation data. *Boundary-Layer Meteorol* 107(2):401–427
- Overland JE, Reynolds RM, Pease CH (1983) A model of the atmospheric boundary layer over the marginal ice zone. *J Geophys Res* 88:2836–2840
- Rasmussen EA, Turner J (eds) (2003) *Polar Lows*. Cambridge University Press, Cambridge, 610 pp

- Renfrew IA, Moore GWK (1999) An extreme cold-air outbreak over the Labrador Sea: roll vortices and air-sea interaction. *Mon Weather Rev* 127(10):2379–2394
- Renfrew IA, King JC (2000) A simple model of the convective internal boundary layer and its application to surface heat flux estimates within polynyas. *Boundary-Layer Meteorol* 94:335–356
- Reynolds M (1984) On the local meteorology at the marginal ice zone of the Bering Sea. *J Geophys Res* 89:6515–6524
- Savijärvi HI (2011) Anti-heat island circulations and low-level jets on a sea gulf. *Tellus A* 63:1007–1013
- Stevens B (2002) Entrainment in stratocumulus-topped mixed layers. *Quart J Roy Meteorol Soc* 128(586):2663–2690
- Venkatram A (1977) A model of internal boundary-layer development. *Boundary Layer Meteorol* 11(4):419–437
- Wacker U, Potty KVJ, Lüpkes C, Hartmann J, Raschendorfer M (2005) A case study on a polar cold air outbreak over Fram Strait using a mesoscale weather prediction model. *Boundary Layer Meteorol* 117(2):301–336
- Yuen C-W (1985) Simulations of cold surges over the oceans with application to AMTEX'75. *J Atmos Sci* 42(2):135–154
- Yuen C-W, Young JA (1986) Dynamical adjustment theory for boundary layer flow in cold surges. *J Atmos Sci* 43(24):3089–3108